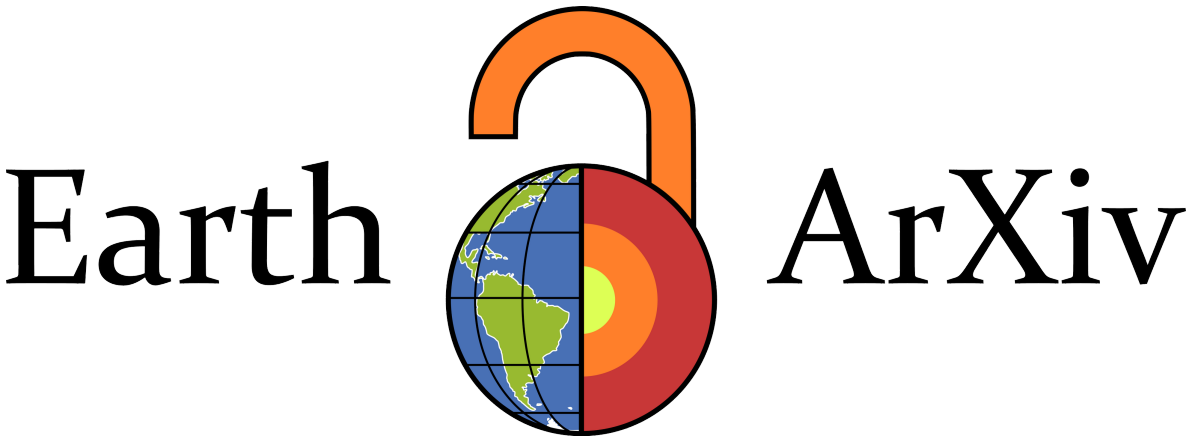

Kelvin-Helmholtz Stability Analysis as a Function of Dipole Tilt and Solar Wind Property

Alexander Navarro[1]*, Xuanye Ma[2], Jay Johnson[1], Simon Wing[3], Shiva Kavosi[4], Yu-Lun Liou[2]

[1] Andrews University, 8975 Old 31, Berrien Springs, MI 49104, USA
[2] Embry-Riddle Aeronautical University, 1 Aerospace Blvd, Daytona Beach, FL 32114, USA
[3] Johns Hopkins University Applied Physics Laboratory, 11100 Johns Hopkins Rd, Laurel, MD 20723, USA
[4] Air Force Research Laboratory, 3550 Aberdeen Ave SE, Kirtland AFB, NM 87117, USA

Kelvin-Helmholtz Stability Analysis as a Function of Dipole Tilt and Solar Wind Property

Alexander Navarro[1*], Xuanye Ma[2], Jay Johnson[1], Simon Wing [3], Shiva Kavosi[4†], Yu-Lun Liou[2]

[1]Andrews University, 8975 Old 31, Berrien Springs, MI 49104
[2]Embry-Riddle Aeronautical University, 1 Aerospace Blvd, Daytona Beach, FL 32114
[3]Johns Hopkins University Applied Physics Laboratory, 11100 Johns Hopkins Rd, Laurel, MD 20723
[4]Air Force Research Lab, 3550 Aberdeen Ave SE, Kirtland AFB, NM 87117

Key Points:

- The KH instability is more pronounced during the equinoxes than during the solstices
- KH instability occurrence is largely insensitive to small IMF magnitudes
- The diurnal dependence of KH occurrence during the summer and winter is consistent with observations.

*Currently at: University of Maryland, 7626 Regents Drive, College Park, MD 20742
†(Pending) Approved for public release, distribution is unlimited. Public Affair release approval.

Corresponding author: Xuanye Ma, max@erau.edu

Abstract

Kelvin-Helmholtz instabilities (KHIs) play a critical role in facilitating mass and momentum transport across the magnetopause boundary. Recent studies have demonstrated that KHI occurrence exhibits both seasonal and diurnal variability, with enhanced activity when Earth's magnetic dipole is more closely aligned with the northward direction in geocentric solar ecliptic (GSE) coordinates (Kavosi et al., 2023). To investigate this behavior, we examine the dependence of KHI stability on the relative orientation of Earth's dipole field and the interplanetary magnetic field (IMF). Using a simplified model of the solar wind, IMF, and Earth's dipolar magnetic field—assuming a parabolic magnetopause geometry—we consider how the draped magnetic field of the Parker spiral and seasonal changes in Earth's dipole orientation modify the stability of the magnetopause boundary and lead to biases and asymmetries in KHI occurrence.

1 Introduction

Driven by the strong flow shear across the magnetopause, the Kelvin-Helmholtz (KH) instability is frequently observed at Earth's magnetopause (Fairfield et al., 2000; K.-J. Hwang et al., 2011; W. Y. Li et al., 2012; K.-J. Hwang et al., 2012; W. Li et al., 2013; Lin et al., 2014; Kavosi & Raeder, 2015; Eriksson et al., 2016; W. Li et al., 2016; Henry et al., 2017; T. Li et al., 2023). As an ideal instability, KH waves facilitate the transfer of momentum and energy between the magnetosheath and magnetosphere (Miura, 1984; Pu & Kivelson, 1983). When the KH instability evolves into its nonlinear stage, the KH vortices can significantly distort the magnetic field, trigger magnetic reconnection, and consequently enable plasma transport from the magnetosheath into the magnetosphere (Fairfield et al., 2000; Otto & Fairfield, 2000; Nykyri & Otto, 2001, 2004; Nakamura & Fujimoto, 2005; Ma et al., 2017; K. Hwang et al., 2020; Ma et al., 2024) (see review in Wing et al. (2014)). Moreover, KH waves can excite kinetic Alfvén waves (KAWs) through mode conversion or coupling processes, providing an additional pathway for cross-boundary energy and plasma transport (Kim et al., 2024). The KH vortices can twist magnetic field lines, generating field-aligned currents (FACs) that play a crucial role in magnetosphere–ionosphere coupling and formation of auroral beads (J. R. Johnson & Wing, 2015; Wing & Johnson, 2015; J. R. Johnson et al., 2021).

With the assumption of incompressibility and an infinitesimally thin boundary layer, Chandrasekhar (1961) demonstrates the KH growth rate as:

$$\gamma^2 = \alpha_1\alpha_2\left[(\mathbf{u}_1-\mathbf{u}_2)\cdot\mathbf{k}\right]^2 - \alpha_1\left(\mathbf{v}_{A1}\cdot\mathbf{k}\right)^2 - \alpha_2\left(\mathbf{v}_{A2}\cdot\mathbf{k}\right)^2, \tag{1}$$

where the subscripts 1 and 2 denote the quantities on each side of the shear boundary layer, $\alpha_i = \rho_i/(\rho_1+\rho_2)$, ρ is the mass density, $\mathbf{u}$ is the bulk velocity, $\mathbf{v}_A = \mathbf{B}/\sqrt{\mu_0\rho}$ is the Alfvén velocity, $\mathbf{B}$ is the magnetic field, μ_0 is the vacuum permeability, $\mathbf{k}$ is KH wavevector. The boundary is KH unstable when $\gamma^2 > 0$. While strong velocity shear enhances the growth rate, a magnetic field component parallel to $\mathbf{k}$ suppresses the instability. Therefore, KH instability is a universal process, which can occur under both northward and southward interplanetary magnetic field (IMF) conditions (Fairfield et al., 2000; Eriksson et al., 2016; K.-J. Hwang et al., 2011; Ma et al., 2014b, 2014a; T. Li et al., 2023) at low latitudes, as well as high latitudes when the IMF is mainly along the dawn-dusk direction (K.-J. Hwang et al., 2012; Ma, Otto, Delamere, & Zhang, 2016; Michael et al., 2021). Furthermore, the KH instability can occur at Venus (Dang et al., 2022), Mars (Poh et al., 2021), Saturn (Masters et al., 2010; Desroche et al., 2013; Ma et al., 2015), Jupiter (Ma et al., 2022; Montgomery et al., 2023), Uranus and Neptune (Donaldson et al., 2024), see detailed discussion by J. Johnson et al. (2014). Recently, Nykyri (2024) showed that the boundary of the coronal mass ejection (CME) impacting Earth's magnetosphere on 10 May 2024—which produced the largest geomagnetic storm in the past two decades—was KH unstable, leading to multi-scale fluctuations in plasma density and magnetic field, including reconnection jets.

Both the solar wind and the planetary magnetic field play crucial roles in the onset of the KH instability; however, most previous studies have primarily focused on the solar wind effect. Kavosi et al. (2023) analyzed one solar cycle of observations from NASA's THEMIS (Time History of Events and Macroscale Interactions during Substorms) and MMS (Magnetospheric Multiscale) missions, revealing that KH instability occurrence rates exhibit distinct seasonal and diurnal variations—being higher near the equinoxes and lower near the solstices. To better understand and quantify this seasonal dependence, it is useful to develop a simple analytical framework. In this study, we employ an idealized magnetopause model to illustrate the seasonal influence on the KH instability. The methodology is described in Section 2, the results are presented in Section 3, the caveats of the approach are discussed in Section 4, and Section 5 provides a summary and concluding remarks.

2 Method

2.1 Paraboloid Model

The solar wind dynamic pressure deforms the shape of the magnetopause so that it is reasonably approximated as a paraboloid (Shue et al., 1997; Joy, 2002; Kanani et al., 2010). Ideally, the normal component of the magnetic field and velocity vanish at the magnetopause boundary. Therefore, it is natural to describe the magnetopause in a three-dimensional parabolic coordinate system, defined as

$$\lambda^2 = \quad r + x \tag{2}$$

$$\mu^2 = \quad r - x \tag{3}$$

$$\tan\phi = \quad z/y, \tag{4}$$

where $r^2 = x^2 + y^2 + z^2$, and (x, y, z) are given in Geocentric Solar Ecliptic (GSE) coordinates.

We employ a current-free dipole field embedded within a paraboloidal magnetopause to isolate the role of dipole tilt in setting the magnetic field orientation and discontinuity across the magnetopause. Chapman–Ferraro currents are captured implicitly through the boundary condition, while internal current systems such as the ring current and field-aligned currents are neglected, as they do not significantly alter the large-scale field geometry governing Kelvin–Helmholtz instability. Since a curl-free magnetic field $\mathbf{B}$ can be written as $\mathbf{B} = -\nabla\Phi$, determining the magnetic field is equivalent to solving Laplace's equation, $\nabla^2\Phi = 0$. In the parabolic coordinate system, Laplace's equation takes the form

$$\frac{1}{\mu^2+\lambda^2}\left[\frac{1}{\mu}\frac{\partial}{\partial\mu}\left(\mu\frac{\partial\Phi}{\partial\mu}\right) + \frac{1}{\lambda}\frac{\partial}{\partial\lambda}\left(\lambda\frac{\partial\Phi}{\partial\lambda}\right)\right] + \frac{1}{\mu^2\lambda^2}\frac{\partial^2\Phi}{\partial\phi^2} = 0. \tag{5}$$

Assuming a boundary at $\lambda = \lambda_0$, the general solution can be expressed as

$$\Phi(\mu,\lambda,\phi) = \sum_{m=-\infty}^{\infty} e^{im\phi} J_m(k\mu) A_m(k) I_m(k\lambda), \tag{6}$$

for the region $\lambda < \lambda_0$, and

$$\Phi(\mu,\lambda,\phi) = \sum_{m=-\infty}^{\infty} e^{im\phi} J_m(k\mu) B_m(k) K_m(k\lambda), \tag{7}$$

for $\lambda > \lambda_0$. Here, J_m denotes the Bessel function of the first kind, while I_m and K_m are the modified Bessel functions of the first and second kinds, respectively (Morse & Feshbach, 1981). In this study, neither the magnetic field nor the velocity is allowed to cross the boundary; therefore, the boundary condition is $\partial_\lambda\Phi = 0$ at $\lambda = \lambda_0 = \sqrt{11.25\,R_\mathrm{E}}$. In our model, we set $\max(\mu) = 5$, which corresponds to $\min(x) = -6.9\,R_\mathrm{E}$ in GSE coordinates. At this location, the tangential magnetosheath velocity is close to the solar

wind speed, and a typical KH wave has already evolved into its nonlinear stage (see our discussion below).

2.1.1 Internal field

Following Stern (1985), the internal field can be expressed as the sum of a dipole field and a shielding field,

$$\Phi_{\rm Int} = \Phi_{\rm dip} + \Phi_{\rm shield}. \tag{8}$$

A dipole with moment $g_{\rm dip}$, tilt angle $\theta_{\rm dip}$, and azimuthal angle $\psi_{\rm dip}$ is located at the origin, while the parabolic coordinates are shifted such that their focus lies at $(x_0, 0, 0)$. In this study, the x_0 is set to be $4.375\,R_{\rm E}$. The dipole potential can be linearly decomposed into components along the x, y, and z directions as

$$\Phi_{\rm dip} = g_{\rm dip}\cos\theta_{\rm dip}\,\Phi_{dz} + g_{\rm dip}\sin\theta_{\rm dip}\cos\psi_{\rm dip}\,\Phi_{dx} + g_{\rm dip}\sin\theta_{\rm dip}\sin\psi_{\rm dip}\,\Phi_{dy}, \tag{9}$$

where the unit-strength dipole potentials in the shifted parabolic coordinate system are given by

$$\Phi_{dx} = 4(\lambda^2 - \mu^2 + 2x_0)\,Q^{-3/2}, \tag{10}$$
$$\Phi_{dy} = 8\lambda\mu\cos\phi\,Q^{-3/2}, \tag{11}$$
$$\Phi_{dz} = 8\lambda\mu\sin\phi\,Q^{-3/2}, \tag{12}$$

and

$$Q = (\lambda^2 + \mu^2)^2 + 4x_0^2 + 4x_0(\lambda^2 - \mu^2). \tag{13}$$

It is therefore sufficient to determine the shielding field associated with a unit-strength dipole in each of the three coordinate directions, subject to the boundary condition $\partial_\lambda\Phi_{si} = -\,\partial_\lambda\Phi_{di}$ at $\lambda = \lambda_0$, to represent the shielding field corresponding to an arbitrary dipole configuration, where $i = x,\, y,\, z$. Note that the x-axis serves as the axis of rotation. Consequently, a dipole with its moment aligned along the x-axis is referred to as the parallel field, whereas dipoles with moments oriented along the y- or z-axis are referred to as perpendicular fields.

Based on the orthogonal Fourier–Bessel expansion, the potential Φ_{si} can be expressed as a series of the form

$$\Phi_{sx} = \sum a_{0n}\,J_0(k_{0n}\mu)\,I_0(k_{0n}\lambda)\,, \tag{14}$$
$$\Phi_{sy} = \cos\phi\sum a_{1n}\,J_1(k_{1n}\mu)\,I_1(k_{1n}\lambda)\,, \tag{15}$$
$$\Phi_{sz} = \sin\phi\sum a_{1n}\,J_1(k_{1n}\mu)\,I_1(k_{1n}\lambda)\,, \tag{16}$$

where k_{0n} and k_{1n} satisfy $J_0(k_{0n}A) = 0$ and $J_1(k_{1n}A) = 0$, respectively. Here, A denotes the truncation range of the expansion. The coefficients a_{0n} and a_{1n} are obtained from the following integrals:

$$a_{0n} = -f_{0n}\int_0^A \mu\left.\frac{\partial\Phi_{dx}}{\partial\lambda}\right|_{\lambda_0} J_0(k_{0n}\mu)\,d\mu, \tag{17}$$
$$f_{0n} = \frac{2}{k_{0n}I_0'(k_{0n}\lambda_0)\,A^2J_1^2(x_{0n})}, \tag{18}$$

and

$$a_{1n} = -f_{1n}\int_0^A \mu\frac{1}{\cos\phi}\left.\frac{\partial\Phi_{dy}}{\partial\lambda}\right|_{\lambda0} J_1(k_{1n}\mu)\,d\mu, \tag{19}$$
$$f_{1n} = \frac{2}{k_{1n}I_1'(k_{1n}\lambda_0)\,A^2J_2^2(x_{1n})}. \tag{20}$$

2.1.2 External field

When the solar wind with a uniform magnetic field encounters the magnetosphere, the field lines are dragged along the magnetopause. Accordingly, the external potential can be decomposed into two components—the uniform potential and the drag potential—such that

$$\Phi_{\rm Ext} = \Phi_{\rm Uni} + \Phi_{\rm Drag}. \tag{21}$$

Similar to the internal field, a uniform IMF potential, with amplitude $g_{\rm IMF}$, polar angle $\theta_{\rm IMF}$, and azimuthal angle $\psi_{\rm IMF}$ can be expressed as a linear combination of three unit-strength potentials,

$$\Phi_{\rm Uni} = g_{\rm IMF}\cos\theta_{\rm IMF}\,\Phi_{uz} + g_{\rm IMF}\sin\theta_{\rm IMF}\cos\psi_{\rm IMF}\,\Phi_{ux} + g_{\rm IMF}\sin\theta_{\rm IMF}\sin\psi_{\rm IMF}\,\Phi_{uy}. \tag{22}$$

Here, the three unit-strength potentials are given by:

$$\Phi_{ux} = x = (\lambda^2-\mu^2)/2, \tag{23}$$
$$\Phi_{uy} = y = \lambda\mu\cos\phi, \tag{24}$$
$$\Phi_{uz} = z = \lambda\mu\sin\phi, \tag{25}$$

Consequently, the drag potential $\Phi_{\rm Drag}$ can be represented by three associated unit-strength components, $\Phi_{{\rm D}x}$, $\Phi_{{\rm D}y}$, and $\Phi_{{\rm D}z}$, each of which can be expressed as a series expansion of the form

$$\Phi_{{\rm D}x} = \sum b_{0n}\,J_0(k_{0n}\mu)\,K_0(k_{0n}\lambda)\,, \tag{26}$$
$$\Phi_{{\rm D}y} = \cos\phi\sum b_{1n}\,J_1(k_{1n}\mu)\,K_1(k_{1n}\lambda)\,, \tag{27}$$
$$\Phi_{{\rm D}z} = \sin\phi\sum b_{1n}\,J_1(k_{1n}\mu)\,K_1(k_{1n}\lambda)\,, \tag{28}$$

where k_{0n} and k_{1n} satisfy $J_0(k_{0n}A)=0$ and $J_1(k_{1n}A)=0$, respectively. Here, A denotes the truncation range of the expansion. The expansion coefficients b_{0n} and b_{1n} are determined from the following integrals:

$$b_{0n} = -f_{0n}\lambda_0\int_0^A \mu J_0(k_{0n}\mu)\,d\mu, \tag{29}$$
$$f_{0n} = \frac{2}{k_{0n}K_0'(k_{0n}\lambda_0)\,A^2J_1^2(x_{0n})}, \tag{30}$$

and

$$b_{1n} = -f_{1n}\int_0^A \mu^2 J_1(k_{1n}\mu)\,d\mu, \tag{31}$$
$$f_{1n} = \frac{2}{k_{1n}K_1'(k_{1n}\lambda_0)\,A^2J_2^2(x_{1n})}, \tag{32}$$

which can be simplified as:

$$b_{0n} = -\frac{2\,\lambda_0}{k_{0n}^2A\,K_0'(k_{0n}\lambda_0)\;J_1(x_{0n})}, \tag{33}$$
$$b_{1n} = \frac{2\,J_0(x_{1n})}{k_{1n}^2\,K_1'(k_{1n}\lambda_0)\;J_2^2(x_{1n})}. \tag{34}$$

Figure 1 shows selected magnetic field lines for external field (blue lines) and internal field (red lines) for parallel potential (A) and perpendicular potential (B). The thick black lines are the magnetopause boundary. Internal or external magnetic fields of any orientation may be constructed using a superposition of the parallel and perpendicular fields shown here. It should be noted that this solution for the external field can also be used to describe the solar wind velocity.

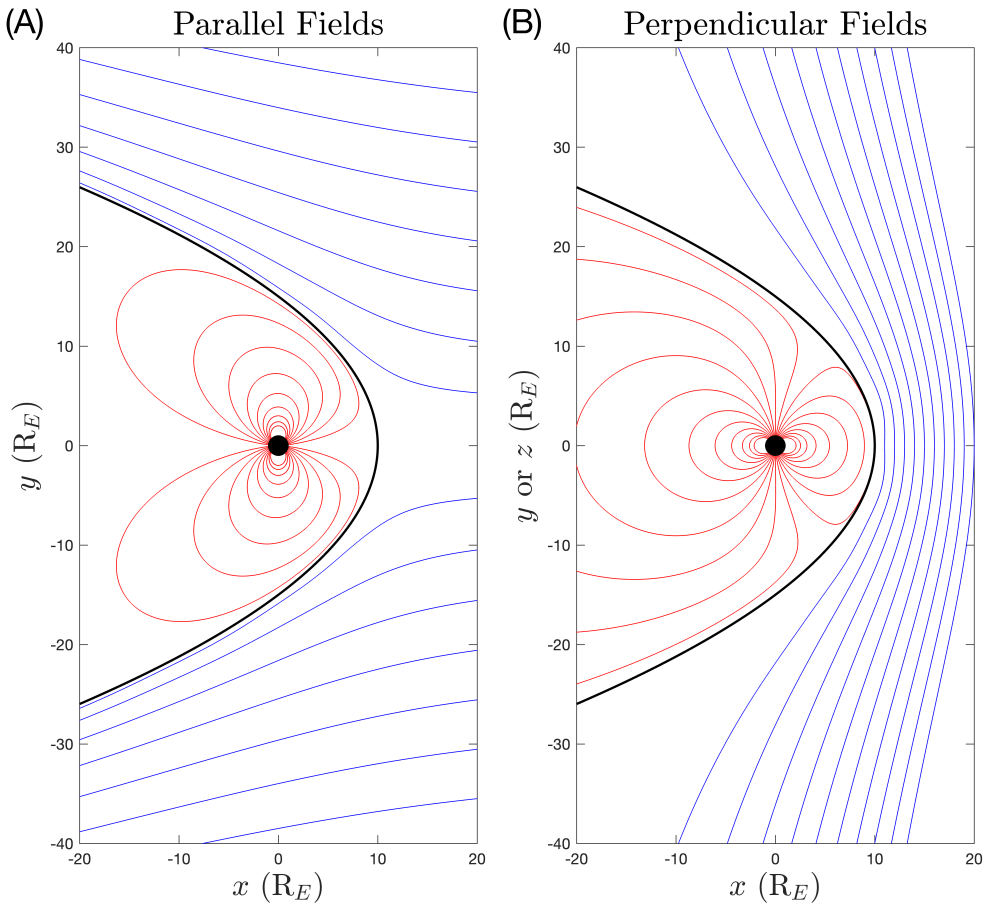

Figure 1. Selected magnetic field lines for external field (blue lines) and internal field (red lines) for parallel potential (A) and perpendicular potential (B). The thick black lines are the magnetopause boundary.

2.1.3 Chapman-Ferraro current

As a byproduct, the tangential discontinuity of the magnetic field at the boundary implies the presence of a surface current—the Chapman–Ferraro current. It can be readily shown that the surface current is

$$\mathbf{I} = \nabla \times (-\Delta\Phi)\,\mathbf{e}_\lambda = \Delta B_\mu\,\mathbf{e}_\phi - \Delta B_\phi\,\mathbf{e}_\mu, \tag{35}$$

where $\Delta F = F_{\rm Ext} - F_{\rm Int}$. Figure 2(A) shows the amplitude of the surface current (color index) at the summer solstice under southward IMF conditions with $B_z = -20\,\mathrm{nT}$. The black lines represent the streamlines of the surface current. The black arrows indicate the direction of surface currents, showing a dawnward current system, which is consistent with the expectation.

2.2 KH onset condition

The KH onset condition (Equation 1) indicates that the growth rate is proportional to the wavenumber k, which is roughly $2\,R_{\rm E}$ to $10\,R_{\rm E}$ at the Earth's magnetopause (Otto & Fairfield, 2000; Lin et al., 2014). The magnitude of the wavelength k is primarily controlled by ion inertia or ion gyroradii at the boundary, as well as by the boundary geometry (see the discussion in Ma (2023)). To isolate the influence of magnetopause properties on the KH mode, we therefore consider the normalized KH growth rate, defined as $\Gamma = \Re(\sqrt{\gamma^2/k^2})$, where $\Re$ denotes the real part of the complex number. Hereafter, Γ is simply referred to as the growth rate. Equation 1 further shows that the growth rate is highly sensitive to the direction of the KH wave vector, $\hat{\mathbf{k}}$. A commonly adopted simplification is to assume that $\mathbf{k}$ is aligned with the direction of the sheared flow. Figure 2(B) presents an example of the square of parallel growth rate, $(\gamma/k_\parallel)^2$ under the same conditions as Figure 2(A), assuming a magnetospheric number density of $5\,\mathrm{cm}^{-3}$ with no background flow and a magnetosheath number density of $20\,\mathrm{cm}^{-3}$ with a flow speed of $250\,\mathrm{km\,s}^{-1}$ at the tailward flank region (i.e., $x = -6.9\,R_{\rm E}$). Hereafter, the same density assumptions are adopted for all other cases. Note that the presence of the dipole tilt angle breaks the north–south symmetry, while the absence of an azimuthal angle in both the magnetosphere and the IMF preserves the dawn–dusk symmetry.

In reality, however, an arbitrary perturbation contains wave components in all directions. For an unstable shear-flow boundary layer, the fastest-growing KH mode corresponds to the direction that maximizes Equation 1, known as the most unstable direction. As demonstrated by Ma (2023), this direction can be readily determined by computing the eigenvector of the symmetric matrix

$$M_{ij} = \alpha_1\alpha_2\Delta u_i\Delta u_j - \alpha_1 v_{A1,i}v_{A1,j} - -\alpha_2 v_{A2,i}v_{A2,j}, \tag{36}$$

where $\Delta\mathbf{u} = \mathbf{u}_1 - \mathbf{u}_2$ is the velocity shear, and the indices i and j denote vector components.

For the magnetopause boundary considered here, the component along the boundary normal is zero. Consequently, the matrix M_{ij} reduces to a 2×2 form, and its eigenvalues can be obtained analytically by solving a quadratic equation. Figure 2(C) shows an example of the square of maximum growth rate, $(\gamma/k_{\rm max})^2$, under the same conditions as Figure 2(B). Both the magnitude and the extent of the unstable region in Figure 2(C) are larger than those in Figure 2(B), which is expected.

As a convective instability, the KH mode propagates from the subsolar magnetopause toward the flank regions. Consequently, the KH waves observed along the magnetopause are likely initiated upstream, and their amplitudes reflect cumulative spatial and temporal growth. To quantify this effect, we integrate the local growth rate along a streamline:

$$\Psi = \int_{\rm subsolr}^{\rm downstream} \Gamma_\parallel / v_g ds \tag{37}$$

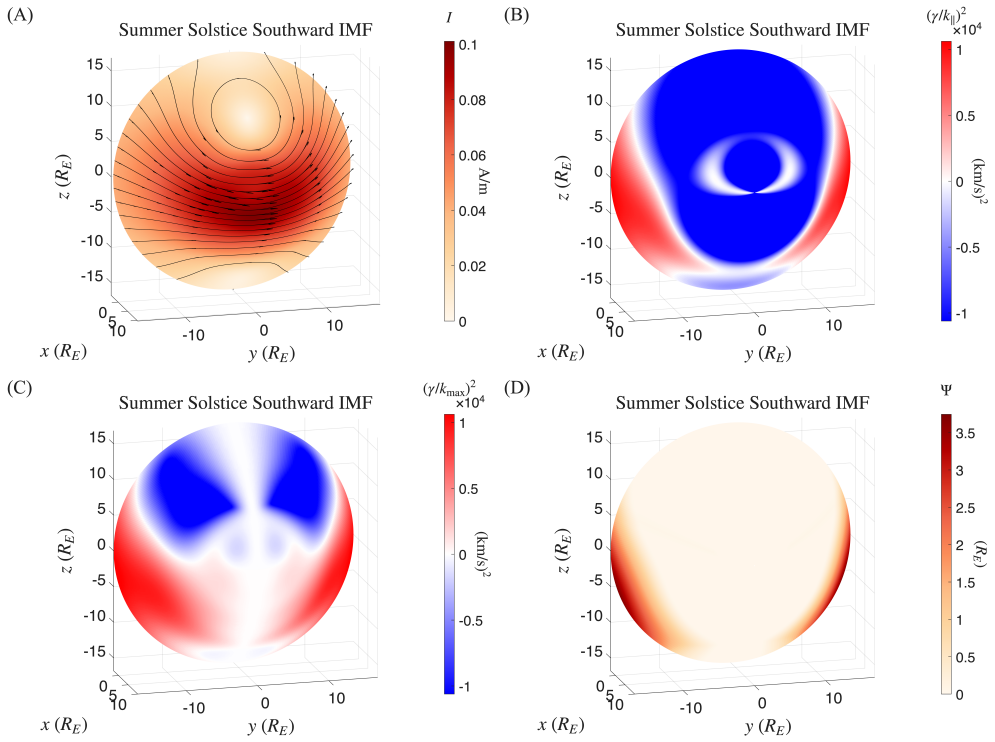

Figure 2. Three-dimensional perspective of the magnetopause boundary at the summer solstice under southward IMF conditions (see context). (A) Amplitude of the surface current (I, color index), with streamlines of the surface current shown in black and arrows indicating its direction. (B) Square of parallel growth rate $(\gamma/k_{\parallel})^2$. (C) Squared of maximum growth rate $(\gamma/k_{\max})^2$. (D) Integrated growth rate, Ψ.

where $v_g = (\rho_1 \mathbf{u}_1 + \rho_2 \mathbf{u}_2)/(\rho_1 + \rho_2)$ is the group velocity of the KH wave along the flow shear direction. This integral is referred to as the integrated growth rate. Figure 2(D) presents an example of Ψ computed for the same parameters as in Figure 2(B), showing that although the KHI can be unstable near the subsolar point (e.g., the white circle near the subsolar point in Figure 2(B)), its cumulative effect is weak. Note that Ψ exceeds $3.5\,R_{\rm E}$ in the tailward flank region. Assuming a KH mode with a wavelength $L \approx 5\,R_{\rm E}$ and a normal velocity perturbation near the subsolar point of $\delta v_n \approx 10\,{\rm km\,s^{-1}}$, the perturbation is expected to grow exponentially as the mode propagates toward the tailward flank region. Specifically, the normal velocity amplitude increases to $\delta v_n \exp(2\pi\Psi/L) \approx 90\,{\rm km\,s^{-1}}$, which is much greater than magnetosheath speed, suggesting that the KH mode has already entered its nonlinear stage. This example illustrates that the integrated growth rate can be interpreted as a measure of the KH mode amplitude.

3 Results

To systematically investigate the influence of seasonal variation on the KH instability under different IMF directions, we compute IMF-probability-weighted averages of the KH growth rate and the integrated growth rate, defined as

$$\overline{F}_P = \int F(\theta_{\rm IMF}, \psi_{\rm IMF}) P(\theta_{\rm IMF}, \psi_{\rm IMF}) d\theta_{\rm IMF} d\psi_{\rm IMF}. \tag{38}$$

Here, F denotes $\Gamma_{\parallel}$, $\max(\Gamma)$, or Ψ, and P represents the probability distribution of the IMF direction as a function of the polar angle $\theta_{\rm IMF}$ and azimuthal angle $\psi_{\rm IMF}$ (see Figure S1 in the supporting information). Note that P exhibits two peak values near $\theta_{\rm IMF} = 0$ and $\psi_{\rm IMF} = -45°$ and 135°, corresponding to the Parker spiral IMF configuration.

If the IMF directional preference is not taken into account, a uniform average over solid angle can be considered, defined as

$$\overline{F}_U = \frac{1}{4\pi} \int F(\theta_{\rm IMF}, \psi_{\rm IMF}) \sin\theta_{\rm IMF} d\theta_{\rm IMF} d\psi_{\rm IMF}. \tag{39}$$

In this paper, we present only results based on $\overline{F}_P$ in the main text; results based on $\overline{F}_U$ are provided in Figure S2 in the supporting information.

Figure 3 shows $\overline{\max(\Gamma)}_P$ (left column) and $\overline{\Psi}_P$ (right column) for the spring equinox, summer solstice, fall equinox, and winter solstice (from top to bottom), for which $\theta_{\rm dip}$ is set to 23° and $\psi_{\rm dip}$ is set to 90°, 0°, −90°, and 180°, respectively. For the solstices, the presence of the tilt angle breaks the north–south symmetry, such that summer conditions preferentially favor the Southern Hemisphere, whereas winter conditions favor the Northern Hemisphere. The preference of the Parker spiral direction in the IMF breaks the dawn–dusk symmetry; however, this asymmetry is relatively weak and is not apparent in $\overline{F}_U$. For the equinoxes, the presence of the azimuthal angle in the magnetosphere further enhances the dawn–dusk asymmetry, with both spring and fall preferentially favoring the dawnside. In contrast, spring conditions favor the Northern Hemisphere, whereas fall conditions favor the Southern Hemisphere. Notably, a peak or multiple peaks appear near the local meridian (defined as the meridian passing through the subsolar point at local noon), slightly offset from the subsolar point, in all $\overline{\max(\Gamma)}_P$ panels, but not in $\overline{\Psi}_P$. This suggests that, if KHI occurs in this region, the wavevector direction is expected to deviate substantially from the flow direction, resulting in a weak cumulative growth effect. These plots further indicate that the equinoxes exhibit larger values of $\overline{\Psi}_P$ than the solstices, suggesting that KHI is more likely to be observed by satellites during spring and fall than during summer and winter, consistent with the statistical analysis of Kavosi et al. (2023).

To illustrate the influence of the IMF magnitude and solar wind speed, we compute the area probability of the integrated growth rate, $P(\Psi)$, defined as

$$P_\Psi = S_\Psi / S, \tag{40}$$

where S_Ψ denotes the area over which the integrated growth rate exceeds Ψ, and S is the total magnetopause surface area.

Figure 4(A) and (B) show the integrated growth rate Ψ as a function of the area probability P_Ψ and the upstream magnetic field magnitude $|B|$ for the spring equinox and summer solstice, respectively, under Parker spiral IMF conditions. Since the fall equinox and winter solstice cases are mirror-symmetric about the equator to the spring equinox and summer solstice cases, respectively, we do not compute these two cases separately. The plots indicate that the KH wave can be significantly compressed when the upstream magnetic field exceeds 15 nT. This effect is more pronounced at the spring equinox. The sudden decrease is consistent with the statistical analysis of Kavosi et al. (2023), who showed that the observed KH occurrence rate is relatively insensitive when the IMF $|B|$ is smaller than 12 nT. One should keep in mind that the external magnetic field considered here is tangential to the magnetopause boundary and is not compressed by the bow shock. Consequently, the magnetic field magnitude shown should not be interpreted as either the IMF or the shocked IMF (i.e., the magnetosheath magnetic field). Because upstream parameters across the bow shock vary substantially, one should not simply assume a fixed compression ratio of 4 to relate the IMF and magnetosheath magnetic field strengths.

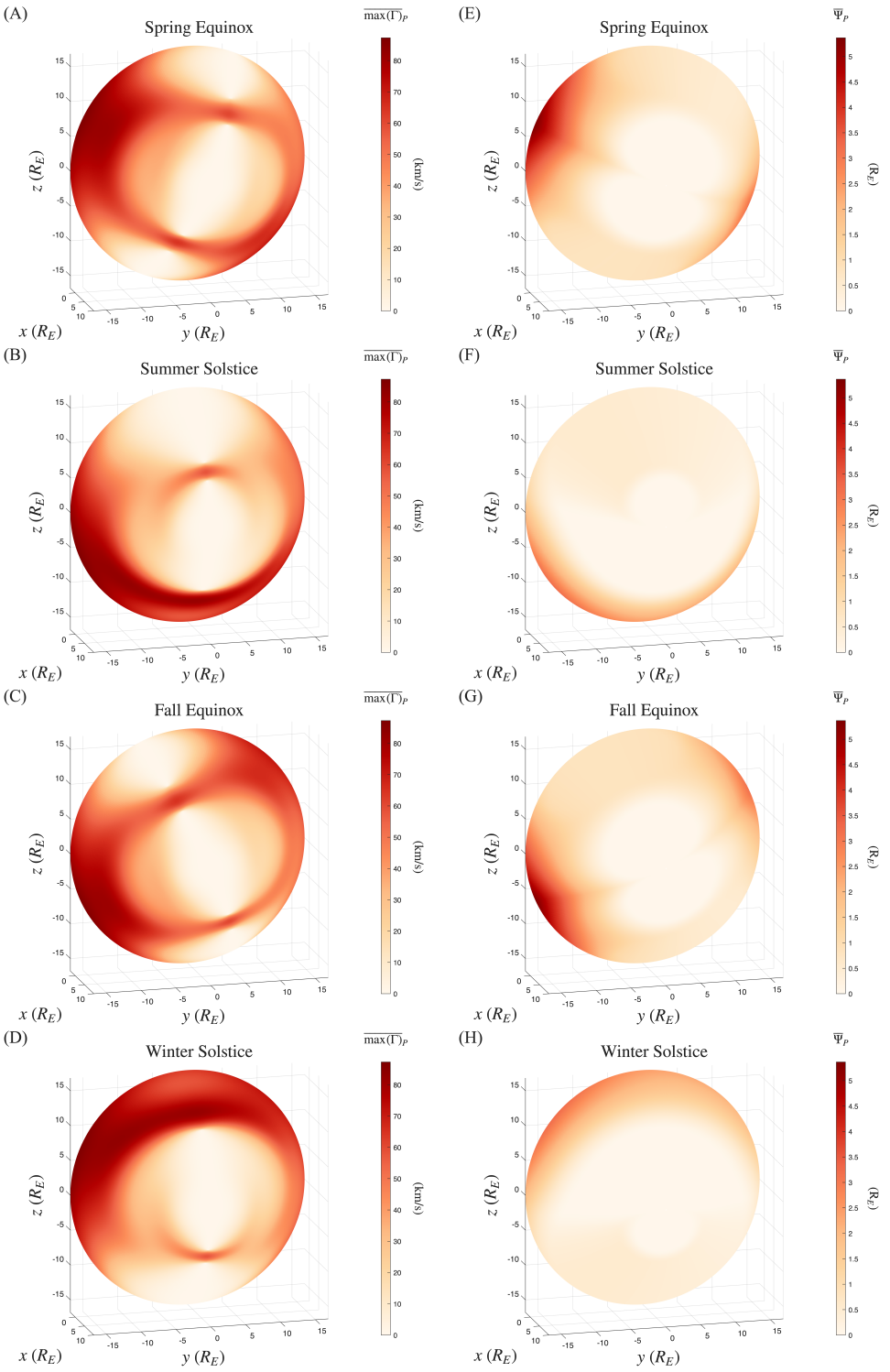

Figure 3. $\overline{\max(\Gamma)}_P$ (left column) and $\overline{\Psi}_P$ (right column) for spring equinox, summer solstice, fall equinox, and winter solstice (from top to bottom).

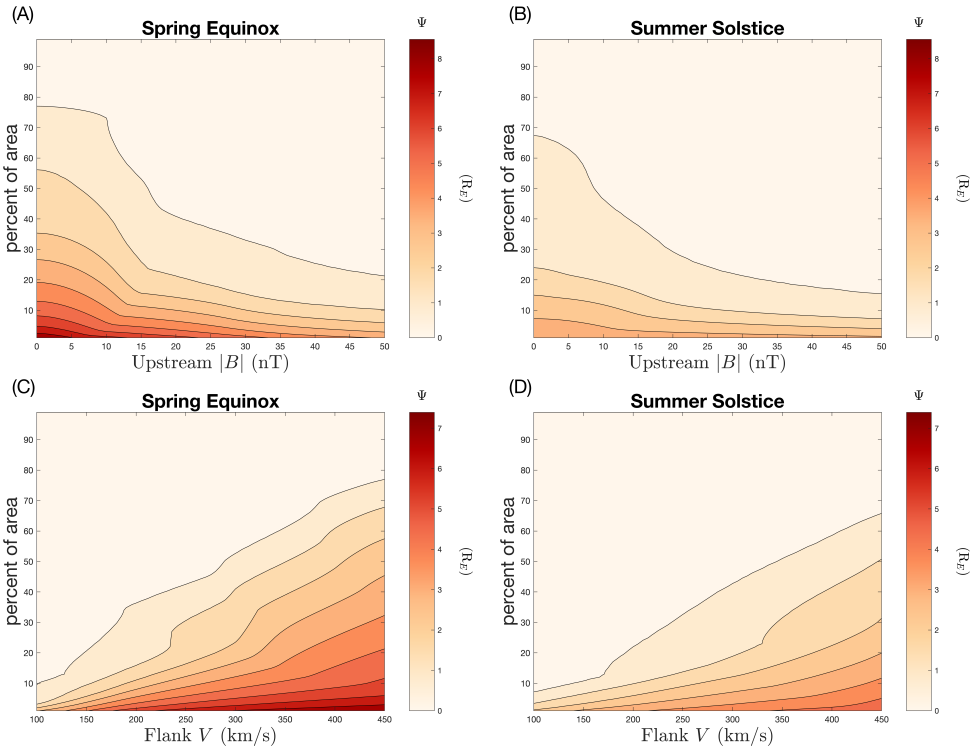

Figure 4. The integrated growth rate Ψ as a function of the area probability P_Ψ and the upstream magnetic field magnitude $|B|$ (top row) and tailward flank region speed V (bottom row), shown for spring equinox (left column) and summer solstice (right column) under Parker spiral IMF conditions.

Figure 4(C) and (D) show the integrated growth rate Ψ as a function of the area probability P_Ψ and the tailward flank region speed V for the spring equinox and summer solstice, respectively, under Parker spiral IMF conditions. These two panels indicate that the KH mode is more likely to be observed under faster solar wind conditions, consistent with the statistical results of Kavosi et al. (2023). However, the growth rates presented here are derived under the incompressibility assumption. In more realistic cases, compressibility effects tend to stabilize the KH mode when the total jump in flow shear exceeds the sum of the fast-mode speeds on both sides of the boundary (Miura, 1982; Ma, Otto, & Delamere, 2016). This effect may partially explain why the observational study of Kavosi et al. (2023) does not find an accelerated enhancement of the KH occurrence rate when the solar wind speed exceeds $350\,\mathrm{km\,s^{-1}}$. In addition, it should be noted that the solar wind speed is nonlinearly anti-correlated with the IMF magnitude (Wing et al., 2016), which can further influence the growth of the KH instability. This anti-correlation may also contribute to the relatively modest increase in the observed KH occurrence rate with increasing solar wind speed, from 11 % to 25 % as the solar wind speed increases from $200\,\mathrm{km\,s^{-1}}$ to $600\,\mathrm{km\,s^{-1}}$.

The Earth's magnetic dipole axis is tilted by approximately 11° relative to the rotation axis, resulting in diurnal variations of its components in the GSE coordinate system due to Earth's rotation. To investigate the influence of this type of diurnal variation on the KH instability, we examine the integrated growth rate Ψ as a function of the area probability P_Ψ and the hour of the day for the spring, summer, fall, and winter sea-

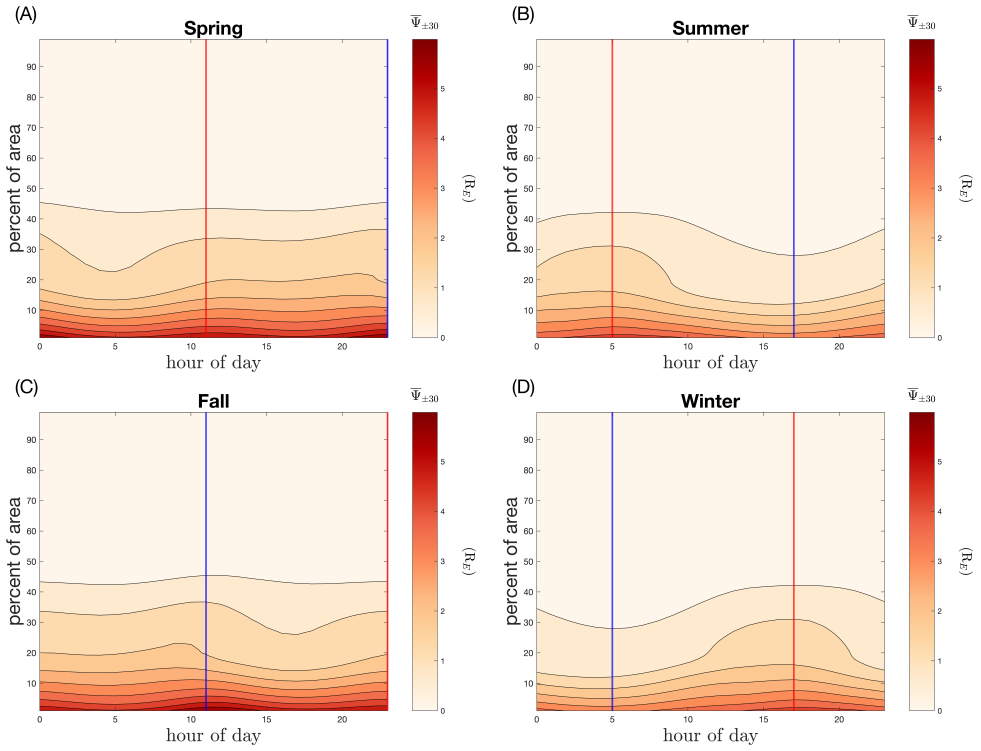

Figure 5. The integrated growth rate Ψ as a function of the area probability and hour of day, shown for spring (A), summer (B), fall (C), and winter (D) under Parker spiral IMF conditions. Blue lines indicate times of maximum dipole tilt, and red lines indicate times of minimum dipole tilt.

sons, respectively, under Parker spiral IMF conditions with $|B| = 20\,\mathrm{nT}$ and a tailward flank speed of $V = 250\,\mathrm{km\,s^{-1}}$. The results are shown in Figure 5. To facilitate comparison with the statistical results of Kavosi et al. (2023), averages are taken over a 30-day window before and after each equinox or solstice. Blue lines indicate times of maximum dipole tilt, whereas red lines indicate times of minimum dipole tilt. In principle, a larger tilt angle implies a stronger magnetic field component along the flow direction, leading to a reduced KHI growth rate. Therefore, the blue and red lines are expected to correspond to the minimum and maximum KH occurrence rates, respectively, which is consistent with the results for summer and winter, as well as with the statistical analysis of Kavosi et al. (2023). However, this simple dependence on the dipole tilt angle is largely smeared out during spring and fall owing to the presence of a larger dipole azimuthal angle. As a result, the integrated growth rate exhibits a weaker diurnal variation during the spring and fall seasons, whereas the statistical results of Kavosi et al. (2023) show a maximum occurrence rate preceding the minimum dipole tilt and a minimum occurrence rate preceding the maximum dipole tilt. One plausible explanation for this discrepancy is that the integrated growth rate depends only weakly on the hour of the day, such that background noise associated with the limited sample size can produce artificial maxima and minima.

4 Summary and discussion

In this study, we employ a simplified analytical magnetopause model to investigate the effects of seasonal and diurnal variations of the dipole tilt angle on the KH instability, as well as the influence of IMF strength and solar wind speed on KH instability. Our main conclusions are summarized as follows.

1. The dipole tilt angle breaks the north–south symmetry, such that KH activity preferentially occurs in the Southern Hemisphere during summer and in the Northern Hemisphere during winter.

2. The dipole and IMF azimuthal angles break the dawn–dusk symmetry. Under Parker spiral IMF conditions, KH activity is enhanced on the dusk side. During the spring equinox, KH instability preferentially occurs in the north–dusk and south–dawn sectors, whereas during the fall equinox it favors the south–dusk and north–dawn sectors.

3. The KH instability is more pronounced during the equinoxes than during the solstices, consistent with the statistical observational study of Kavosi et al. (2023).

4. Although the KH instability can be locally unstable near the subsolar point, its cumulative effect there is weak.

5. A weak IMF maintains instability along the low-latitude boundary, resulting in KH occurrence that is largely insensitive to small IMF magnitudes, while faster solar wind speeds enhance KH instability across the entire magnetopause. Both features are mostly consistent with the statistical observational results of Kavosi et al. (2023).

6. The diurnal dependence of KH occurrence exhibits clear seasonal variation. The summer and winter patterns are consistent with observations. In contrast, small-amplitude KH waves during spring and fall show weak diurnal modulation, suggesting that reported KH occurrence rates during these seasons are more susceptible to observational biases.

Although our simplified analytical model mostly agrees with observational statistical results in many respects, several important caveats should be noted.

1. The KH growth rate used in this study (i.e., Equation 1 is derived under a local slab geometry assumption. In reality, the flow shear increases with distance from the subsolar point, and the magnetic field exhibits curvature away from the equatorial plane. These global-scale geometric effects can influence the growth of the KH instability but are not included in Equation 1. A more sophisticated treatment would formulate the entire magnetopause as a boundary-value problem and solve for the corresponding eigenmodes. However, such an eigenmode analysis requires a force-balanced magnetopause model. While force balance can, in principle, be achieved in the normal direction, the presence of tangential flow continuously advects and bends magnetic flux from upstream to downstream, making it difficult to maintain a steady force balance. As a result, whether a strictly steady-state magnetopause boundary exists remains an open question.

2. In this study, we consider KH waves with wave vectors parallel to the flow direction when calculating the integrated growth rate, since the KH group velocity propagates predominantly in the same direction. In reality, KH instability can also develop for wave vectors oblique to the flow. Determining the group velocity for a dispersion relation with both real and imaginary components is beyond the scope of this study. Moreover, even if the group velocity could be accurately determined, it remains unclear how KH waves propagate along the magnetopause when their wave vectors deviate from the direction of the flow shear. A fundamental resolution of this issue again requires solving the global eigenmode problem for the entire magnetopause.

3. As discussed above, the KH onset condition adopted in this study is based on the incompressibility assumption. Miura and Pritchett (1982) analyzed the KH insta-

bility for compressible plasmas and finite initial shear layer widths, showing that the growth rate does not increase monotonically with decreasing wavelength and that sufficiently strong flow shear can, in fact, suppress the instability. We do not adopt this more complete treatment here because of its substantially higher computational cost. Nevertheless, KH wavelengths at the Earth's magnetopause are typically much larger than the initial shear layer width, and compressibility effects mainly become important for extremely fast flow shear, which is relatively rare at the terrestrial magnetopause. Therefore, despite its simplifications, our model captures the essential physics and is able to reproduce key observational features.

Open Research Section

This study is entirely theoretical and does not rely on satellite or observational data. All equations, model assumptions, and numerical procedures are explicitly documented in the manuscript and supporting information.

Acknowledgments

The authors acknowledge funding from NASA grants 80NSSC22K0515, 80NSSK230899, 80NSSC21K1321, 80NSSC21K2009, 80NSSC22K0310, 80NSSC22K0515, 80NSSC22K0311, and NSF grants AGS2131013, AGS2247395, AGS2431664, AGS2307203, and AGS2308853. The views expressed are those of the authors and do not reflect the official guidance or position of the United States Government, the Department of Defense or of the United States Air Force. The appearance of external hyperlinks does not constitute endorsement by the United States Department of Defense (DoD) of the linked websites, or the information, products, or services contained therein. The DoD does not exercise any editorial, security, or other control over the information you may find at these locations.

References

Chandrasekhar, S. (1961). *Hydrodynamic and hydromagnetic stability*. Dover Publ. Retrieved from http://books.google.com/books?id=oU_-6ikmidoC

Dang, T., Lei, J., Zhang, B., Zhang, T., Yao, Z., Lyon, J., ... Merkin, V. (2022, March). Oxygen Ion Escape at Venus Associated With Three-Dimensional Kelvin-Helmholtz Instability. *Geophysical Research Letters*, *49*(6). Retrieved 2022-10-26, from https://onlinelibrary.wiley.com/doi/10.1029/2021GL096961 doi: 10.1029/2021GL096961

Desroche, M., Bagenal, F., Delamere, P. A., & Erkaev, N. (2013, June). Conditions at the magnetopause of Saturn and implications for the solar wind interaction. *Journal of Geophysical Research (Space Physics)*, *118*, 3087–3095. doi: 10.1002/jgra.50294

Donaldson, K., Olsen, A. J., Paty, C. S., & Caggiano, J. (2024, August). Characterizing the Solar Wind-Magnetosphere Viscous Interaction at Uranus and Neptune. *Journal of Geophysical Research: Space Physics*, *129*(8), e2024JA032518. Retrieved 2025-10-27, from https://agupubs.onlinelibrary.wiley.com/doi/10.1029/2024JA032518 doi: 10.1029/2024JA032518

Eriksson, S., Lavraud, B., Wilder, F. D., Stawarz, J. E., Giles, B. L., Burch, J. L., ... Goodrich, K. A. (2016). Magnetospheric Multiscale observations of magnetic reconnection associated with Kelvin-Helmholtz waves. *Geophysical Research Letters*, *43*(11), 5606–5615. Retrieved from http://dx.doi.org/10.1002/2016GL068783 doi: 10.1002/2016GL068783

Fairfield, D. H., Otto, A., Mukai, T., Kokubun, S., Lepping, R. P., Steinberg, J. T., ... Yamamoto, T. (2000). Geotail observations of the Kelvin-Helmholtz instability at the equatorial magnetotail boundary for parallel northward fields. *Journal of Geophysical Research*, *105*, 21159–21174. doi:

10.1029/1999JA000316

Henry, Z. W., Nykyri, K., Moore, T. W., Dimmock, A. P., & Ma, X. (2017). On the dawn-dusk asymmetry of the kelvin-helmholtz instability between 2007 and 2013. *Journal of Geophysical Research: Space Physics*, *122*(12), 11,888–11,900. Retrieved from https://agupubs.onlinelibrary.wiley.com/doi/abs/10.1002/2017JA024548 doi: https://doi.org/10.1002/2017JA024548

Hwang, K., Dokgo, K., Choi, E., Burch, J. L., Sibeck, D. G., Giles, B. L., ... Strangeway, R. J. (2020, April). Magnetic Reconnection Inside a Flux Rope Induced by Kelvin-Helmholtz Vortices. *Journal of Geophysical Research: Space Physics*, *125*(4). Retrieved 2023-05-23, from https://onlinelibrary.wiley.com/doi/10.1029/2019JA027665 doi: 10.1029/2019JA027665

Hwang, K.-J., Goldstein, M. L., Kuznetsova, M. M., Wang, Y., ViñAs, A. F., & Sibeck, D. G. (2012, August). The first in situ observation of Kelvin-Helmholtz waves at high-latitude magnetopause during strongly dawnward interplanetary magnetic field conditions. *Journal of Geophysical Research (Space Physics)*, *117*, 8233. doi: 10.1029/2011JA017256

Hwang, K.-J., Kuznetsova, M. M., Sahraoui, F., Goldstein, M. L., Lee, E., & Parks, G. K. (2011, August). Kelvin-Helmholtz waves under southward interplanetary magnetic field. *Journal of Geophysical Research*, *116*(A15), 8210. doi: 10.1029/2011JA016596

Johnson, J., Wing, S., & Delamere, P. (2014). Kelvin Helmholtz instability in planetary magnetospheres. *Space Science Reviews*, *184*(1-4), 1–31. Retrieved from http://dx.doi.org/10.1007/s11214-014-0085-z doi: 10.1007/s11214-014-0085-z

Johnson, J. R., & Wing, S. (2015, May). The dependence of the strength and thickness of field-aligned currents on solar wind and ionospheric parameters. *Journal of Geophysical Research: Space Physics*, *120*(5), 3987–4008. Retrieved 2023-10-13, from https://agupubs.onlinelibrary.wiley.com/doi/10.1002/2014JA020312 doi: 10.1002/2014JA020312

Johnson, J. R., Wing, S., Delamere, P., Petrinec, S., & Kavosi, S. (2021). Field-aligned currents in auroral vortices. *Journal of Geophysical Research: Space Physics*, *126*(2), e2020JA028583. Retrieved from https://agupubs.onlinelibrary.wiley.com/doi/abs/10.1029/2020JA028583 doi: https://doi.org/10.1029/2020JA028583

Joy, S. P. (2002). Probabilistic models of the Jovian magnetopause and bow shock locations. *Journal of Geophysical Research*, *107*(A10), 1309. Retrieved 2023-10-10, from http://doi.wiley.com/10.1029/2001JA009146 doi: 10.1029/2001JA009146

Kanani, S. J., Arridge, C. S., Jones, G. H., Fazakerley, A. N., McAndrews, H. J., Sergis, N., ... Krupp, N. (2010, June). A new form of Saturn's magnetopause using a dynamic pressure balance model, based on in situ, multi-instrument Cassini measurements. *Journal of Geophysical Research (Space Physics)*, *115*(A14), 6207–+. Retrieved from http://dx.doi.org/10.1029/2009JA014262 doi: 10.1029/2009JA014262

Kavosi, S., & Raeder, J. (2015, May). Ubiquity of kelvin-helmholtz waves at earth's magnetopause. *Nature Communications*, *6*, 7019. doi: 10.1038/ncomms8019

Kavosi, S., Raeder, J., Johnson, J. R., Nykyri, K., & Farrugia, C. J. (2023, May). Seasonal and diurnal variations of Kelvin-Helmholtz Instability at terrestrial magnetopause. *Nature Communications*, *14*(1), 2513. Retrieved 2023-05-23, from https://www.nature.com/articles/s41467-023-37485-x doi: 10.1038/s41467-023-37485-x

Kim, E., Johnson, J. R., & Damiano, P. A. (2024, May). Alfvén Waves at the Interface of Solar Wind and Magnetosphere. In A. Keiling (Ed.), *Geophysical Monograph Series* (1st ed., pp. 249–267). Wiley. Retrieved 2025-10-27, from https://agupubs.onlinelibrary.wiley.com/doi/10.1002/

9781394195985.ch11 doi: 10.1002/9781394195985.ch11

Li, T., Li, W., Tang, B., Khotyaintsev, Y. V., Graham, D. B., Ardakani, A., ... Wang, C. (2023, October). Kelvin-Helmholtz Waves and Magnetic Reconnection at the Earth's Magnetopause Under Southward Interplanetary Magnetic Field. *Geophysical Research Letters*, *50*(20), e2023GL105539. Retrieved 2023-12-27, from https://agupubs.onlinelibrary.wiley.com/doi/10.1029/2023GL105539 doi: 10.1029/2023GL105539

Li, W., André, M., Khotyaintsev, Y. V., Vaivads, A., Graham, D. B., Toledo-Redondo, S., ... Strangeway, R. J. (2016). Kinetic evidence of magnetic reconnection due to Kelvin-Helmholtz waves. *Geophysical Research Letters*, *43*(11), 5635–5643. Retrieved from http://dx.doi.org/10.1002/2016GL069192 doi: 10.1002/2016GL069192

Li, W., Wang, C., Tang, B., Guo, X., & Lin, D. (2013, August). Global features of Kelvin-Helmholtz waves at the magnetopause for northward interplanetary magnetic field. *Journal of Geophysical Research (Space Physics)*, *118*, 5118–5126. doi: 10.1002/jgra.50498

Li, W. Y., Guo, X. C., & Wang, C. (2012, August). Spatial distribution of Kelvin-Helmholtz instability at low-latitude boundary layer under different solar wind speed conditions. *Journal of Geophysical Research (Space Physics)*, *117*, 8230. doi: 10.1029/2012JA017780

Lin, D., Wang, C., Li, W., Tang, B., Guo, X., & Peng, Z. (2014). Properties of Kelvin-Helmholtz waves at the magnetopause under northward interplanetary magnetic field: Statistical study. *Journal of Geophysical Research: Space Physics*, *119*(9), 7485–7494. Retrieved from http://dx.doi.org/10.1002/2014JA020379 doi: 10.1002/2014JA020379

Ma, X. (2023, August). Estimation of the Kelvin-Helmholtz Unstable Boundary. *Journal of Geophysical Research: Space Physics*, *128*(8), e2023JA031602. Retrieved 2023-10-13, from https://agupubs.onlinelibrary.wiley.com/doi/10.1029/2023JA031602 doi: 10.1029/2023JA031602

Ma, X., Delamere, P., Nykyri, K., Otto, A., Eriksson, S., Chai, L., ... Kavosi, S. (2024, March). Density and Magnetic Field Asymmetric Kelvin-Helmholtz Instability. *Journal of Geophysical Research: Space Physics*, *129*(3), e2023JA032234. Retrieved 2024-03-18, from https://agupubs.onlinelibrary.wiley.com/doi/10.1029/2023JA032234 doi: 10.1029/2023JA032234

Ma, X., Delamere, P., Otto, A., & Burkholder, B. (2017). Plasma transport driven by the three-dimensional Kelvin-Helmholtz instability. *Journal of Geophysical Research: Space Physics*, *122*(10), 10,382–10,395. Retrieved from https://agupubs.onlinelibrary.wiley.com/doi/abs/10.1002/2017JA024394 doi: https://doi.org/10.1002/2017JA024394

Ma, X., Delamere, P. A., Schok, A., Wing, S., Johnson, J. R., & Liou, Y. (2022, October). Jupiter's Sheared Flow Unstable Magnetopause Boundary Observed by Juno. *Journal of Geophysical Research: Space Physics*, *127*(10). Retrieved 2022-10-26, from https://onlinelibrary.wiley.com/doi/10.1029/2022JA030719 doi: 10.1029/2022JA030719

Ma, X., Otto, A., & Delamere, P. A. (2014a). Interaction of magnetic reconnection and Kelvin-Helmholtz modes for large magnetic shear: 1. Kelvin-Helmholtz trigger. *Journal of Geophysical Research: Space Physics*, *119*(2), 781–797.

Ma, X., Otto, A., & Delamere, P. A. (2014b). Interaction of magnetic reconnection and Kelvin-Helmholtz modes for large magnetic shear: 2. Reconnection trigger. *Journal of Geophysical Research: Space Physics*, *119*(2), 808–820.

Ma, X., Otto, A., & Delamere, P. A. (2016). Magnetic reconnection with a fast perpendicular sheared flow. *Journal of Geophysical Research: Space Physics*, *121*(10), 9427–9442.

Ma, X., Otto, A., Delamere, P. A., & Zhang, H. (2016). Interaction between reconnection and Kelvin-Helmholtz at the high-latitude magnetopause.

Advances in Space Research, *58*(2), 231–239. Retrieved from https://www.sciencedirect.com/science/article/pii/S0273117716300047 doi: https://doi.org/10.1016/j.asr.2016.02.025

Ma, X., Stauffer, B., Delamere, P. A., & Otto, A. (2015). Asymmetric Kelvin-Helmholtz propagation at Saturn's dayside magnetopause. *Journal of Geophysical Research: Space Physics*, *120*(3), 1867–1875. Retrieved from http://dx.doi.org/10.1002/2014JA020746 doi: 10.1002/2014JA020746

Masters, A., Achilleos, N., Kivelson, M. G., Sergis, N., Dougherty, M. K., Thomsen, M. F., ... Coates, A. J. (2010, July). Cassini observations of a Kelvin-Helmholtz vortex in Saturn's outer magnetosphere. *Journal of Geophysical Research: Space Physics*, *115*(A7), 2010JA015351. Retrieved 2023-10-09, from https://agupubs.onlinelibrary.wiley.com/doi/10.1029/2010JA015351 doi: 10.1029/2010JA015351

Michael, A. T., Sorathia, K. A., Merkin, V. G., Nykyri, K., Burkholder, B., Ma, X., ... Garretson, J. (2021, October). Modeling Kelvin-Helmholtz Instability at the High-Latitude Boundary Layer in a Global Magnetosphere Simulation. *Geophysical Research Letters*, *48*(19). Retrieved 2023-02-27, from https://onlinelibrary.wiley.com/doi/10.1029/2021GL094002 doi: 10.1029/2021GL094002

Miura, A. (1982). Nonlinear evolution of the magnetohydrodynamic Kelvin-Helmholtz instability. *Physical Review Letters*, *49*, 779.

Miura, A. (1984, February). Anomalous transport by magnetohydrodynamic Kelvin-Helmholtz instabilities in the solar wind-magnetosphere interaction. *Journal of Geophysical Research*, *89*, 801–818. doi: 10.1029/JA089iA02p00801

Miura, A., & Pritchett, P. L. (1982, September). Nonlocal stability analysis of the MHD Kelvin-Helmholtz instability in a compressible plasma. *Journal of Geophysical Research*, *87*, 7431–7444. doi: 10.1029/JA087iA09p07431

Montgomery, J., Ebert, R. W., Allegrini, F., Bagenal, F., Bolton, S. J., DiBraccio, G. A., ... Masters, A. (2023, July). Investigating the Occurrence of Kelvin-Helmholtz Instabilities at Jupiter's Dawn Magnetopause. *Geophysical Research Letters*, *50*(14), e2023GL102921. Retrieved 2023-10-10, from https://agupubs.onlinelibrary.wiley.com/doi/10.1029/2023GL102921 doi: 10.1029/2023GL102921

Morse, P. M., & Feshbach, H. (1981). Methods of theoretical physics. 2: Chapters 9 to 13. In (Renewed ed.). Minneapolis: Feshbach Publ.

Nakamura, T. K. M., & Fujimoto, M. (2005, November). Magnetic reconnection within rolled-up MHD-scale Kelvin-Helmholtz vortices: Two-fluid simulations including finite electron inertial effects. *Geophysical Research Letters*, *32*, 21102. doi: 10.1029/2005GL023362

Nykyri, K. (2024, April). On the Importance of the Kelvin-Helmholtz Instability on Magnetospheric and Solar Wind Dynamics During High Magnetic Shear. *Geophysical Research Letters*, *51*(8), e2024GL108605. Retrieved 2024-10-22, from https://agupubs.onlinelibrary.wiley.com/doi/10.1029/2024GL108605 doi: 10.1029/2024GL108605

Nykyri, K., & Otto, A. (2001, September). Plasma transport at the magnetospheric boundary due to reconnection in Kelvin-Helmholtz vortices. *Geophysical Research Letters*, *28*, 3565–3568. doi: 10.1029/2001GL013239

Nykyri, K., & Otto, A. (2004, March). Influence of the Hall term on KH instability and reconnection inside KH vortices. *Annales Geophysicae*, *22*, 935–949. doi: 10.5194/angeo-22-935-2004

Otto, A., & Fairfield, D. H. (2000). Kelvin-Helmholtz instability at the magnetotail boundary: MHD simulation and comparison with Geotail observations. *Journal of Geophysical Research*, *105*, 21175–21190. doi: 10.1029/1999JA000312

Poh, G., Espley, J. R., Nykyri, K., Fowler, C. M., Ma, X., Xu, S., ... DiBraccio, G. A. (2021, September). On the Growth and Development of Non-Linear

Kelvin-Helmholtz Instability at Mars: MAVEN Observations. *Journal of Geophysical Research: Space Physics*, *126*(9). Retrieved 2022-10-26, from https://onlinelibrary.wiley.com/doi/10.1029/2021JA029224 doi: 10.1029/2021JA029224

Pu, Z.-Y., & Kivelson, M. G. (1983). Kelvin-Helmholtz Instability at the magnetopause: Energy flux into the magnetosphere. *Journal of Geophysical Research: Space Physics*, *88*(A2), 853–861. Retrieved from https://agupubs.onlinelibrary.wiley.com/doi/abs/10.1029/JA088iA02p00853 doi: https://doi.org/10.1029/JA088iA02p00853

Shue, J.-H., Chao, J. K., Fu, H. C., Russell, C. T., Song, P., Khurana, K. K., & Singer, H. J. (1997, May). A new functional form to study the solar wind control of the magnetopause size and shape. *Journal of Geophysical Research: Space Physics*, *102*(A5), 9497–9511. Retrieved 2023-04-16, from http://doi.wiley.com/10.1029/97JA00196 doi: 10.1029/97JA00196

Stern, D. P. (1985, November). Parabolic harmonics in magnetospheric modeling: The main dipole and the ring current. *Journal of Geophysical Research: Space Physics*, *90*(A11), 10851–10863. Retrieved 2025-11-04, from https://agupubs.onlinelibrary.wiley.com/doi/10.1029/JA090iA11p10851 doi: 10.1029/JA090iA11p10851

Wing, S., & Johnson, J. R. (2015, November). Theory and observations of upward field-aligned currents at the magnetopause boundary layer. *Geophysical Research Letters*, *42*(21), 9149–9155. Retrieved 2023-10-13, from https://agupubs.onlinelibrary.wiley.com/doi/10.1002/2015GL065464 doi: 10.1002/2015GL065464

Wing, S., Johnson, J. R., Camporeale, E., & Reeves, G. D. (2016). Information theoretical approach to discovering solar wind drivers of the outer radiation belt. *Journal of Geophysical Research: Space Physics*, *121*(10), 9378–9399. Retrieved from https://agupubs.onlinelibrary.wiley.com/doi/abs/10.1002/2016JA022711 doi: https://doi.org/10.1002/2016JA022711

Wing, S., Johnson, J. R., Chaston, C. C., Echim, M., Escoubet, C. P., Lavraud, B., ... Wang, C.-P. (2014, November). Review of Solar Wind Entry into and Transport Within the Plasma Sheet. *Space Science Reviews*, *184*(1-4), 33–86. Retrieved 2023-03-04, from http://link.springer.com/10.1007/s11214-014-0108-9 doi: 10.1007/s11214-014-0108-9

Supporting Information for "Kelvin-Helmholtz Stability Analysis as a Function of Dipole Tilt and Solar Wind Property"

Alexander Navarro[1], Xuanye Ma[2], Jay Johnson[1], Simon Wing [3], Shiva Kavosi[4], Yu-Lun Liou[2]

[1]Andrews University, 8975 Old 31, Berrien Springs, MI 49104

[2]Embry-Riddle Aeronautical University, 1 Aerospace Blvd, Daytona Beach, FL 32114

[3]Johns Hopkins University Applied Physics Laboratory, 11100 Johns Hopkins Rd, Laurel, MD 20723

[4]Air Force Research Lab, 3550 Aberdeen Ave SE, Kirtland AFB, NM 87117

Contents of this file

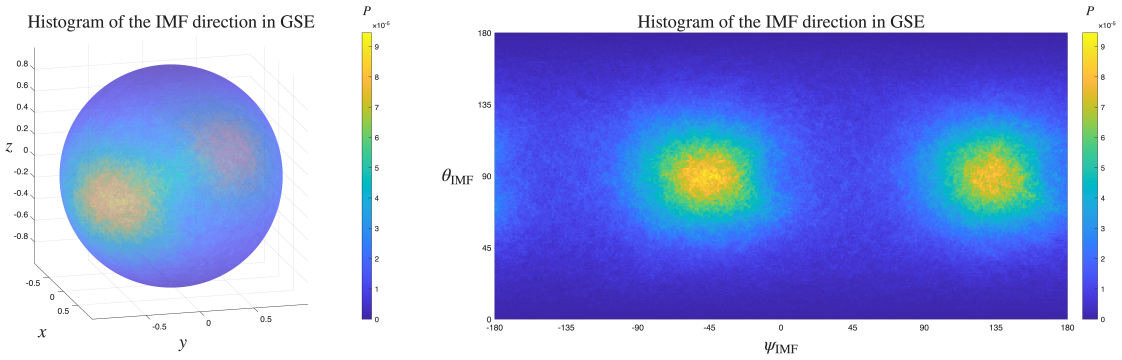

Figure S1. Histogram of the IMF direction in GSE coordinates, shown in a three-dimensional view (left) and in the $\theta_{\rm IMF}$–$\psi_{\rm IMF}$ plane (right).

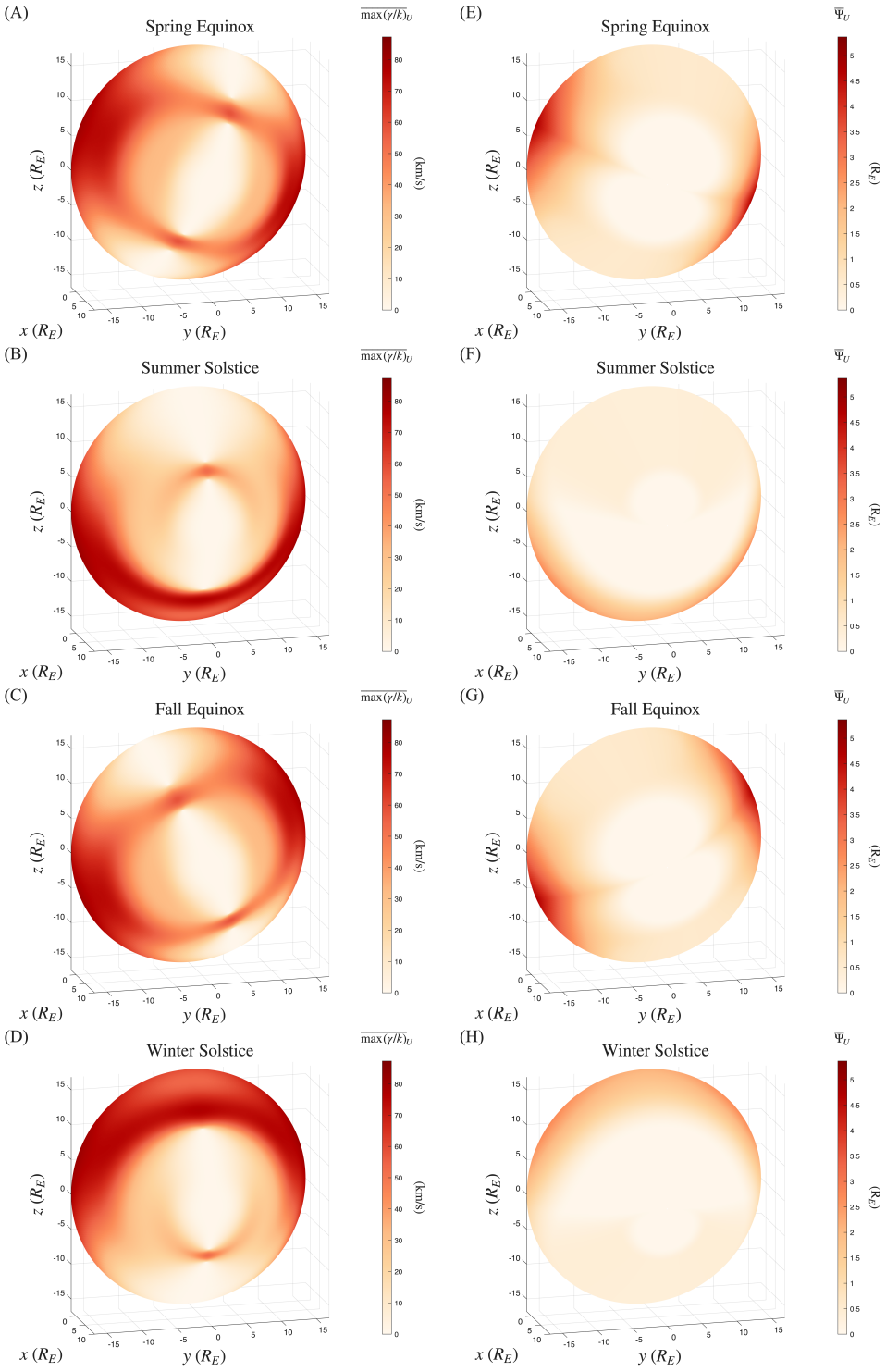

Figure S2. $\overline{\max(\Gamma)}_U$ (left column) and $\overline{\Psi}_U$ (right column) for spring equinox, summer solstice, fall equinox, and winter solstice (from top to bottom).